Verification of Remotely Sensed Sea Surface Winds in Hurricanes

ERIC W. UHLHORN

University of Miami, RSMAS/CIMAS, Miami, Florida

PETER G. BLACK

NOAA/AOML/Hurricane Research Division, Miami, Florida

(Manuscript received 16 April 2002, in final form 31 July 2002)

ABSTRACT

Surface winds in hurricanes have been estimated remotely using the Stepped-Frequency Microwave Radiometer (SFMR) from the NOAA WP-3D aircraft for the past 15 years. Since the use of the GPS dropwindsonde system in hurricanes was first initiated in 1997, routine collocated SFMR and GPS surface wind estimates have been made. During the 1998, 1999, and 2001 hurricane seasons, a total of 249 paired samples were acquired and compared. The SFMR equivalent 1-min mean, 10-m level neutral stability winds were found to be biased high by 2.3 m s^{-1} relative to the 10-m GPS winds computed from an estimate of the mean boundary layer wind. Across the range of wind speeds from 10 to 60 m s^{-1}, the rmse was 3.3 m s^{-1}. The bias was found to be dependent on storm quadrant and independent of wind speed, a result that suggests a possible relationship between microwave brightness temperatures and surface wave properties. Tests of retrieved winds' sensitivities to sea surface temperature, salinity, atmospheric thermodynamic variability, and surface wind direction indicate wind speed errors of less than 1 m s^{-1} above 15 m s^{-1}.

1. Introduction

Measurement of the hurricane surface wind field, and in particular the estimation of wind maxima, has long been a requirement of the Tropical Prediction Center/National Hurricane Center (TPC/NHC). This paper describes the validation of remotely sensed sea surface winds from the Hurricane Research Division's (HRD) Stepped-Frequency Microwave Radiometer (SFMR). The first experimental SFMR surface wind measurements were made in Hurricane Allen in 1980, the first real-time retrieval of winds on board the aircraft in Hurricane Earl in 1985, and the first operational transmission of winds to TPC/NHC in Hurricane Dennis in 1999. SFMR wind speeds are compared with independent measurements from Global Positioning System (GPS) dropwindsondes from the 1998, 1999, and 2001 hurricane seasons.

Since hurricane reconnaissance began in 1947, numerous methods have been employed to estimate the distribution of surface winds in hurricanes. Sea state catalogs have provided a guide to determination of the wind speed (Black and Adams 1983). For many years surface winds have been estimated by flight-level measurements using various extrapolation algorithms (Powell et al. 1996; Powell 1980; Miller 1958). Maximum sustained winds have been estimated using pressure–wind relationships by Kraft (1961) and more recently by Dvorak (1984). Studies prior to 1980 (Ross and Cardone 1974; Nordberg et al. 1969) have shown that passive microwave emissions from the sea surface are also strongly correlated with wind speed.

The concept for the first experimental SFMR was proposed by C. T. Swift at the University of Massachusetts Microwave Remote Sensing Laboratory (C. T. Swift 1976, personal communication) and built by the National Aeronautics and Space Administration's (NASA) Langley Research Center in 1978 (Harrington 1980). The SFMR design involved a single nadir-viewing antenna and receiver capable of making measurements of radio emission from the sea surface at four selectable frequencies between 4.5 and 7.2 GHz. The ''stepping'' procedure allowed for estimating the surface wind speed in hurricanes by correcting for rain-induced effects in the measurements, and therefore enabling recovery of the rain rate. The first measurements by the original SFMR were made from the National Oceanic and Atmospheric Administration (NOAA) WC-130 aircraft in Hurricane Allen in 1980 and reported in Jones et al. (1981), as well as Black and Swift (1984), Delnore et al. (1985), and Swift and Goodberlet (1992). By making assumptions about the vertical structure of the at-

Corresponding author address: Eric W. Uhlhorn, University of Miami, RSMAS/CIMAS, 4301 Rickenbacker Cswy., Miami, FL 33149.
E-mail: Eric.Uhlhorn@noaa.gov

mosphere together with SST measurements by a downward-looking airborne infrared radiometer, reasonable estimates of the ocean surface brightness temperature (T_B) were made at 4.5, 5.0, 5.6, and 6.6 GHz. Wind speeds were then calculated assuming a linear increase in wind speed with T_B, independent of frequency. Agreement between surface (20 m) winds extrapolated from the 1500-m flight level and the SFMR estimates for independent flight legs were within ±10%. Despite the success in Allen, this instrument was never again flown into a hurricane.

A second SFMR was designed and built in 1982 under the supervision of Swift (Swift et al. 1986). The number of frequencies was expanded to six between 4.6 and 7.2 GHz, and the instrument integration time was reduced to less than 1 s, resulting in improved spatial resolution. A new retrieval algorithm was also implemented and described in Tanner et al. (1987). This instrument was flown on board the NOAA WP-3D in 1984 and during 12 flights during the 1985 hurricane season. The SFMR was further modified in 1986 and initially used for studies of sea ice structure (St. Germain et al. 1993). Using data obtained in Hurricanes Earl (1985), Gilbert (1988), and Hugo (1989), the empirical emissivity–wind speed relationships were refined to include winds over 60 m s^{-1}.

With support from the Office of the Federal Coordinator for Meteorology (OFCM) the existing horn antenna was replaced with a dipole array antenna in 1993. The new antenna with a new set of six frequencies was flown in Hurricane Olivia (1994) and retrieved high quality wind estimates. Further funds were provided by OFCM for an upgrade of the SFMR's receiver, which allowed for increased calibration stability. The reconfigured SFMR (Goodberlet and Swift 1996) was first flown in Hurricane Jerry in 1995. Minor modifications were made to reduce background noise levels after the 1995 season, and since then the SFMR has flown under this configuration. Following component failures in 2000, the NOAA Office of Oceanic and Atmospheric Research supported an instrument repair and again the SFMR returned surface winds during the 2001 hurricane season. Since 1980, the SFMR has flown on 95 flights in 30 tropical cyclones.

In 1997, hurricane research missions began obtaining atmospheric wind and thermodynamic profiles with GPS dropwindsondes (Hock and Franklin 1999). The advent of GPS sonde measurements marked a vast improvement in the accuracy of winds (both magnitude and location) within the boundary layer. Here, we compare SFMR 1-min equivalent surface wind measurements with wind speeds at 10-m height derived from GPS sondes. Due to advection the GPS sonde and SFMR paired surface wind speed samples are generally displaced some distance.

The purpose of this study is threefold: 1) to quantitatively demonstrate that the winds estimated by the SFMR now represent an important operational tool for mapping the distribution of surface winds in hurricanes; 2) to establish an unprecedented independent validation of remotely sensed sea surface wind speeds between 10 m s^{-1} and in excess of 50 m s^{-1}; and 3) to relate the natural variability of the atmosphere and ocean to errors in the retrieved meteorological parameter of interest (i.e., surface wind speed). In this paper, section 2 explains the methodology used to obtain and process concurrent GPS–SFMR surface wind measurements. The results of the comparisons are presented in section 3. Section 4 describes a radiative transfer model sensitivity analysis. A discussion of the results is presented in section 5 and section 6 contains concluding remarks. In the appendices, a brief theory of microwave radiometry and its application to the SFMR is presented, and a discussion is given of SFMR system specifications, calibration procedures, and estimates of instrument noise.

2. Data processing methodology

The HRD SFMR measures radiative emissions, expressed in terms of a brightness temperature (T_B), from several sources including the ocean and the atmosphere, at six frequencies from 4.55 to 7.22 GHz. The percentage of foam coverage on the sea surface increases monotonically with wind speed (Barrick and Swift 1980). At microwave frequencies, foam is approximately a blackbody; therefore, as foam increases, the ocean emits microwave energy more readily and, assuming a constant sea surface temperature, T_B increases (Webster et al. 1976). Given an accurate physical model that relates ocean surface wind speed to measurements of T_B at several frequencies, a set of simultaneous equations may, in theory, be inverted to calculate the surface wind under practically all weather conditions (see appendix A for details).

A wind speed estimate is computed from the set of SFMR T_B measured at a rate of 1 Hz, although truly independent measurements are possible only at a much slower sampling rate, 0.1 Hz. The dependence of microwave emissivity on small-scale ocean roughness at nadir incidence angle is weak (Rosenkranz and Staelin 1972). Therefore, the SFMR is fairly insensitive (small change in T_B per unit wind speed change) at wind speeds less than ~10 m s^{-1}, since little sea foam is generated, and the inversion algorithm often fails to converge to a unique solution. Surface winds <10 m s^{-1} are not included.

The algorithm recognizes measurements entirely over land, where typically $T_B \geq 280$ K, but when land partially fills the radiometer footprint or sidelobes, a false wind speed retrieval can occur. Measurements within 10 km of land are not considered in the data comparisons.

Observations of T_B are restricted to vertical incidence by removing data where the aircraft rolls and/or pitches >2°. Often particular channels are contaminated by radio frequency interference (RFI) from ground-based

sources (e.g., communications and weather radar). Prior to solving for the wind speed, each channel is checked for RFI by passing the set of T_B measurements through a median filter. Values that fall outside a threshold based upon the average deviation are not used in the calculation. A minimum of two channels are required to solve the system of equations, but the algorithm requires at least three of six in order to reduce errors.

For comparison with the GPS surface wind, SFMR measurements representative of the wind speed at 10-m altitude are sought. A 1-min average SFMR value is calculated by a running mean wind speed convolved with a triangular (Bartlett) data window to reduce sidelobe influence. Each of the independent variables (time and location) are lagged to correspond to the filtered wind speed value.

The P-3 aircraft routinely deploys GPS dropwindsondes. Among other variables, the GPS dropwindsonde measures horizontal wind vector components at ~5 m vertical resolution. The sondes often fail to measure winds all the way to the sea surface, especially under the highest wind conditions. Thus for comparison purposes an approximation of the 10-m wind is made from the lowest 500-m mean (MBL) wind speed measured by the sonde. A set of 590 paired samples of MBL and 10-m winds have been obtained, denoted as G_{MBL} and G_{10}, respectively. All measurements are over ocean and the sample is well distributed among storm quadrants, radial distance from storm center, latitude, and storm strength. A linear least squares best fit yields

$$G_{10} = 0.798(G_{\mathrm{MBL}}). \quad (1)$$

This fit compares reasonably well to the typical 20% reduction of flight-level (1–3 km) winds previously used to estimate surface winds in hurricanes (Powell 1980). The rmse of this estimate is 2.49 m s^{-1}. A plot of the MBL and 10-m wind speed paired samples used to develop the relationship is shown in Fig. 1. Recent results from analyses of GPS wind measurements in hurricanes (Dunion et al. 2002, manuscript submitted to *Mon. Wea. Rev.*, hereafter DLH) now indicate a general tendency to underestimate 10-m winds relative to the MBL wind at both low (<20 m s^{-1}) and high (>55 m s^{-1}) winds using extrapolation procedures commonly used. Evidence of this phenomenon also exists in the GPS wind data compiled for this study. Surface winds are slightly underestimated by the regression equation at speeds <15–20 m s^{-1}, and >60 m s^{-1}. Since the SFMR is not as responsive at the low wind speed range, the underestimation is not a great concern, but it may be more important when estimating the highest winds.

Until now nothing has been said of the averaging time inherent in the GPS surface wind estimates. TPC/NHC refers wind speed measurements to a ''maximum one minute sustained wind''; a 1-min average wind speed is estimated by the SFMR using a running mean of the surface wind measurements. The GPS sondes sample as they follow flow trajectories, and relating the four-dimensional Lagrangian statistical variability to a more familiar Eulerian description is extremely difficult. Thus the space scales and timescales of motion that are represented by the GPS measurements are still a topic of debate. Recent work has shown (DLH; Powell et al. 1996), however, that the MBL wind is approximately equivalent to a 5-min averaging period and may be converted to a 1-min maximum sustained wind by multiplying by an ~6% ''gust factor.'' How this adjustment affects the intercomparison will be addressed in the next section.

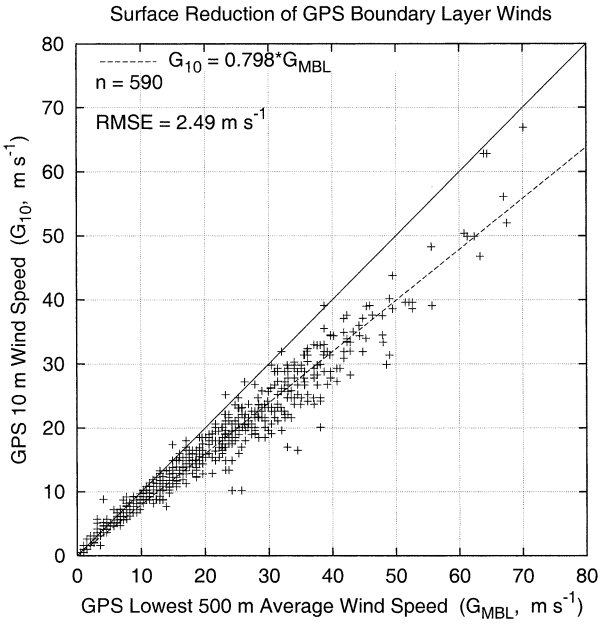

FIG. 1. Relationship between GPS-measured mean boundary layer wind speed and 10-m wind speed. The least squares best fit is indicated by the dashed line, and the solid line represents perfect correlation.

3. Verification results

a. Approach

A total of 249 paired samples of SFMR and surface-adjusted GPS MBL winds were obtained from 1998, 1999, and 2001, as reflected in the scatterplot in Fig. 2. To be included, paired observations had to be within 15 km total distance of each other and within 10 km radially with respect to the storm center. The least squares best fit to the data is

$$S_{10} = 2.68 + 0.98(G_{10}), \quad (2)$$

where S_{10} is the surface wind speed (m s^{-1}) measured by the SFMR. The degree of scatter about this fit is characterized by an rmse of 3.31 m s^{-1}. Generally, the remotely sensed surface wind is overestimated relative to the 10-m GPS measurement, nearly independent of the magnitude.

The corresponding histogram of the distribution of

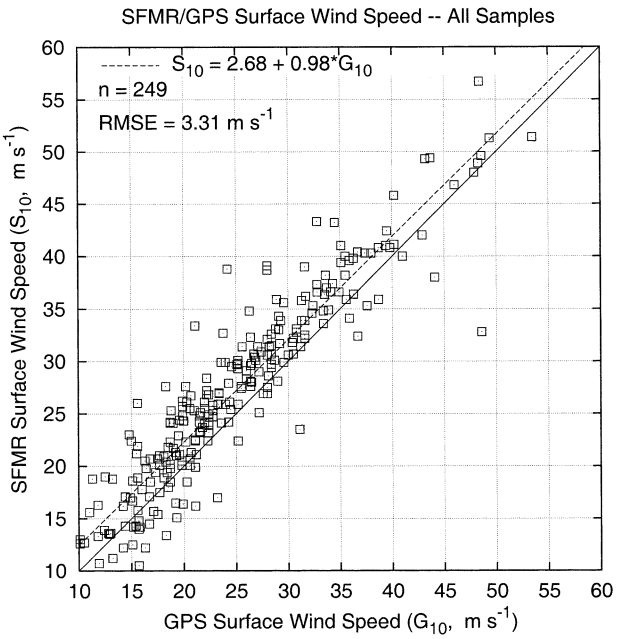

FIG. 2. SFMR–GPS surface wind speed comparisons for all samples. The solid line indicates perfect correlation and the dashed line indicates the best fit.

errors, defined as SFMR minus GPS, is plotted in Fig. 3. The high positive skewness ($=+1.4$) of the frequency distribution reveals the increased likelihood of overestimation with respect to the mean bias of $\mu = +2.33$ m s^{-1}. The cumulative frequency indicates that the middle 50% of the errors range between approximately 0 and $+4$ m s^{-1}.

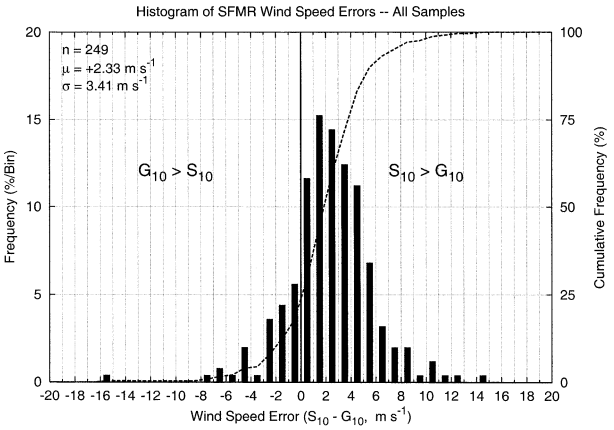

FIG. 3. Histogram of SFMR wind speed errors relative to GPS surface wind speed for all samples. For the $n = 249$ observations the mean error is $\mu = +2.33$ m s^{-1} with a std dev of $\sigma = 3.41$ m s^{-1}. The cumulative frequency distribution is indicated by the dashed line.

To assess the source of the outlying data points, a subset of the full sample is constructed whereby storms of significant asymmetric structure are removed. Also, the locations of each of the hurricanes during which GPS drops were made concurrently with the SFMR operating vary widely; many of the samples are in regions of significant currents such as the Gulf Stream. Accordingly, measurements near continental coastlines and over the Gulf Stream are deleted to eliminate possible current and shoaling effects. The geographical locations of the sample pairs of wind measurements are plotted in Fig. 4.

Shown in Fig. 5 are data for the 76 measurements

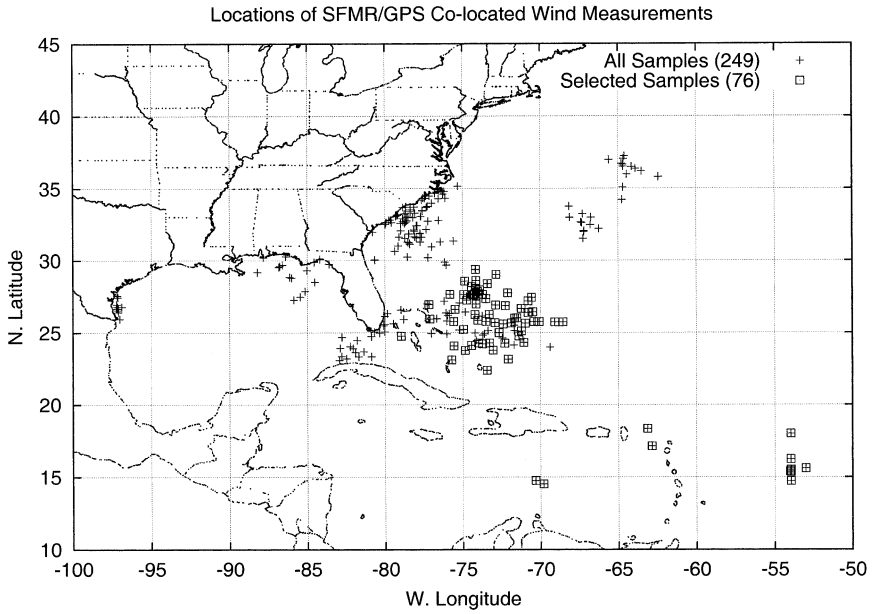

FIG. 4. Geographic locations of wind measurements used in this study. The $n = 249$ full sample is indicated by (+) and the $n = 76$ subset is indicated by (□).

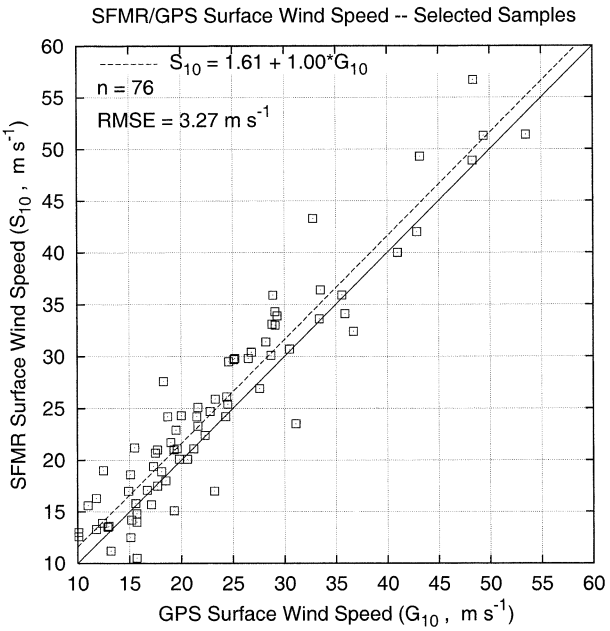

FIG. 5. SFMR–GPS wind speed comparisons of selected samples. The solid line indicates perfect correlation and the dashed line indicates the best fit.

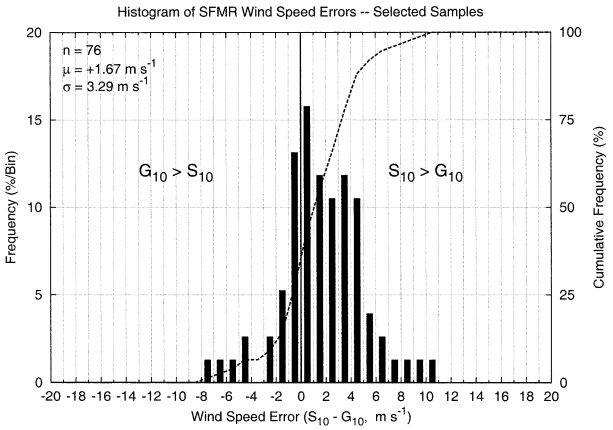

FIG. 6. Histogram of SFMR wind speed errors relative to GPS surface wind speed for selected samples. For the $n = 76$ observations the mean error is $\mu = +1.67$ m s^{-1} with std dev of $\sigma = 3.29$ m s^{-1}. The cumulative frequency distribution is indicated by the dashed line.

that satisfied these criteria. The least squares best fit for this sample is $S_{10} = 1.61 + 1.00(G_{10})$, with rmse of 3.27 m s^{-1}. Several outliers were removed, and there is still a tendency for overestimation. Both the bias and the variance of the errors are slightly reduced in the selected subsample, as indicated by the histogram of errors in Fig. 6. The following analyses focus on this particular subsample.

DLH have argued that increasing the surface-adjusted MBL wind speed by around 6% is the equivalent time average of a 1-min maximum sustained wind speed at 10 m. The apparent high bias of the SFMR versus GPS measurements may be due to the differences in the timescales implicit in the measurements. It is interesting to note that by increasing the mean wind speed in the dataset ($\sim$27 m s^{-1}) by 6% would give nearly exactly the 1.6 m s^{-1} high bias in Fig. 5. Additionally, the fact that the GPS surface winds may be underestimated by the MBL wind at high wind speeds would also lead to decreasing the bias. It must still be noted, however, that for winds $<$55 m s^{-1}, the gust factor adjustment is less than the rmse ($=$3.27 m s^{-1}) of the SFMR versus GPS comparison.

b. Radial dependence of errors

To improve our understanding of the error distribution, the data have been analyzed according to their radial distance r from the center of tropical cyclones as described by the ''best-track'' (Jarvinen et al. 1984) data from NHC, supplemented with available radar observations. For each radial traverse, a radius of maximum wind (r_0) is identified from the SFMR data. A mean of these r_0 for each storm is used to normalize r for the paired samples.

As was shown in Fig. 5, the mean measurement error is essentially independent of the wind speed. Surface winds in hurricanes generally decrease with radial distance from the radius of maximum wind ($r/r_0 = 1$), so we ask whether this independence of error exists radially as well. Wind speed errors, again defined here as SFMR minus GPS, are plotted as a function of r/r_0 in Fig. 7. A decrease is seen in the SFMR's overestimation with increased distance from the storm center. By contrast there is little error dependence on wind speed.

c. Storm quadrant dependence of errors

When each paired sample is located in a rotated polar coordinate system such that 0° is in the direction of storm motion, the spatial distribution of samples is as shown in Fig. 8 for both the entire ($n = 249$) sample and the selected ($n = 76$) sample set. Paired samples are next binned according to quadrant of storm, and differences between SFMR and GPS wind speed measurements are computed for each quadrant. A mean difference of $S_{10} - G_{10} = 3.53$ m s^{-1} is found in the left rear (LR) quadrant, while in the right rear (RR) we find an overestimation by the SFMR of 0.30 m s^{-1}. As shown in Table 1, the results of a Student's t-test indicate a statistically significant difference in quadrant bias (Δbias) at the 99% level occurs between the LR and RR quadrants.

Wind speed differences between SFMR and GPS, plotted as a function of azimuth angle with respect to the direction of storm motion, are shown in Fig. 9. Based on averages computed for 30° bins, a fairly clear harmonic signal is revealed. Although more measurements are necessary to truly quantify the significance, it is apparent that some process independent of the local sur-

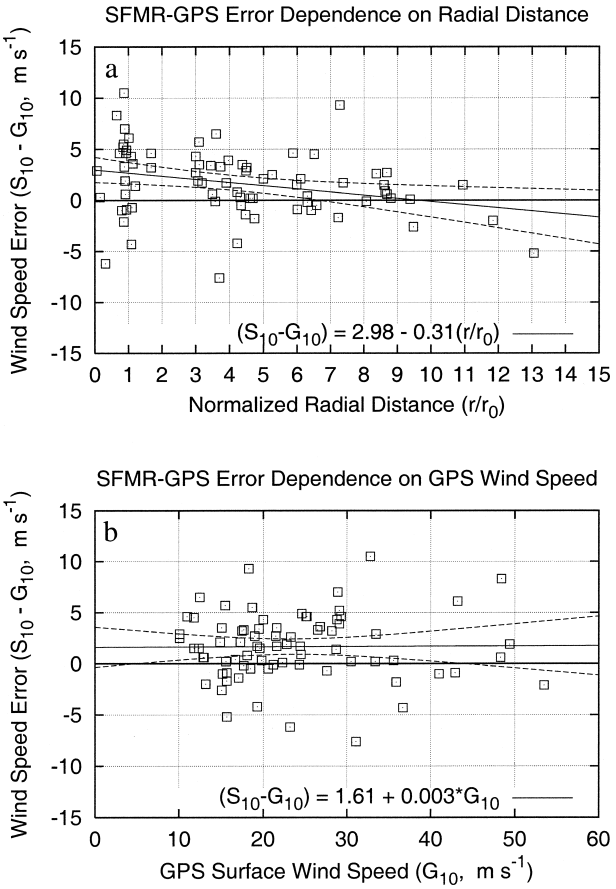

FIG. 7. SFMR wind speed error relative to surface truth GPS wind speed (m s^{-1}) plotted (a) as a function of normalized radial distance (r/r_0) from center of storms (dimensionless), and (b) as a function of GPS surface wind speed (m s^{-1}). Linear regressions along with 95% confidence limits are indicated.

face wind speed may be responsible for discrepancies in the SFMR-derived wind in hurricanes.

Previous studies have speculated on the relationship between foam coverage and fetch length (e.g., Martsinkevich and Melent'ev 1982; Webster et al. 1976; Ross and Cardone 1974). The physical explanation is related to the stage of wave development (i.e., the wave energy spectral distribution) and the resulting production of whitecaps and subsequent foam patches upon wave breaking. Thus an increase in T_B may depend at least partly on the sea state and not purely upon the local surface wind. Based on the observations of previous authors, one hypothesis that may explain the underestimate of surface winds in the RR quadrant of storms (LR in the Southern Hemisphere) is that the fetch length limitation is linked to decreased foam coverage, leading to a tendency to underestimate the local surface wind. In the RR quadrant, by contrast, the sea is still in an active building stage and the shorter, higher-frequency waves that persist in this fetch-limited region are not producing the large foam patches upon breaking, at least in an average sense relative to other regions of the storm.

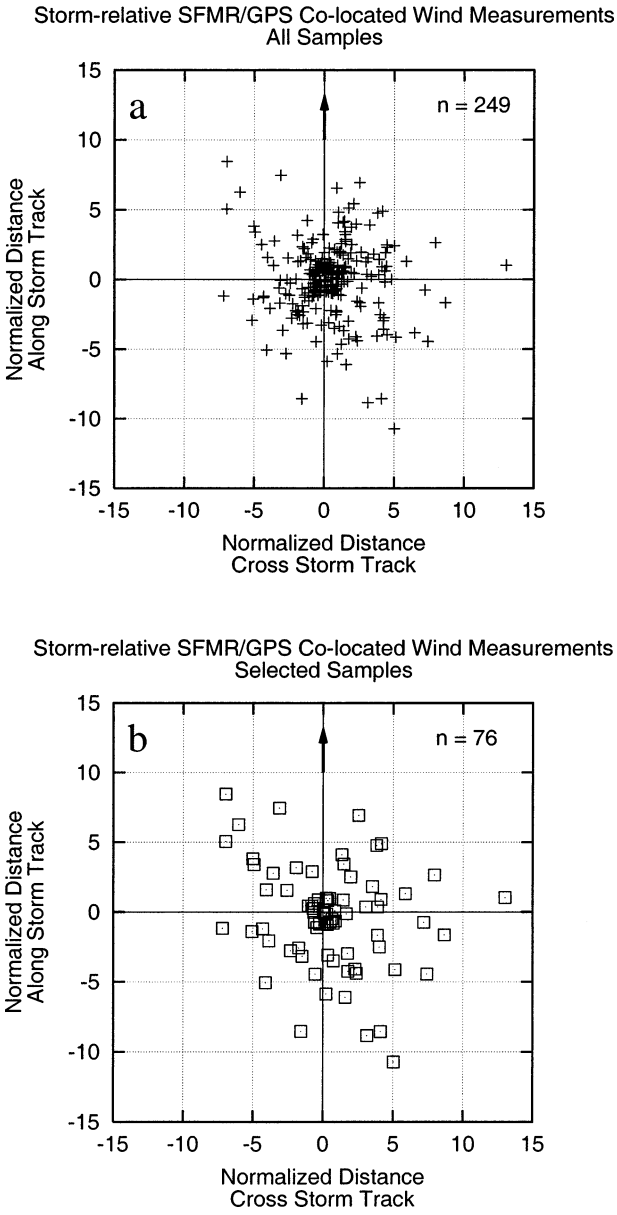

FIG. 8. Storm-relative locations of SFMR–GPS wind speed comparisons for the (a) entire and (b) selected sample sets. The direction of storm motion is indicated by the arrow.

TABLE 1. Comparison of significance of differences in biases (SFMR − GPS) among quadrants, ranked by |Δbias|. The left column indicates the two quadrants for which the biases are compared. The significance level of the differences in biases based on the Student's t-test are shown in the right column.

Quads.	Δbias	Sig. level
RR–LR	−3.23	99
RF–RR	+1.65	90
LF–LR	−1.60	<90
RF–LR	−1.58	<90
LF–RR	+0.63	<90
LF–RF	−0.02	<90

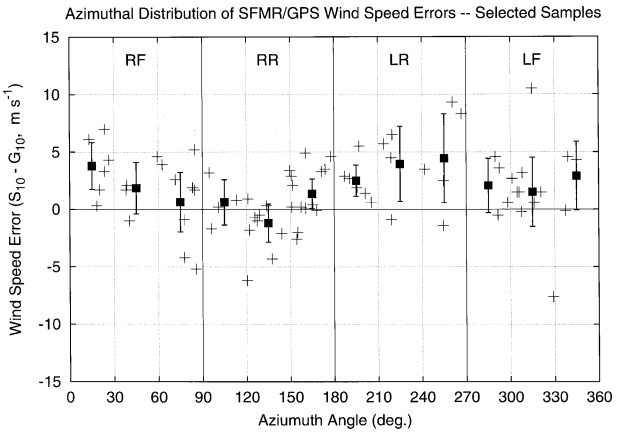

FIG. 9. Polar distribution of SFMR–GPS wind speed errors. Storm quadrant is indicated at the top. Also plotted are the mean values computed for 30° bins along with 95% confidence limits on the mean.

4. Sensitivity analysis

In this section, a sensitivity analysis is presented on the errors in the SFMR wind speed estimates associated with assumptions made in the microwave radiative transfer problem. As mentioned in section 2, the apparent ocean T_B from which the wind speed is derived includes radiative contributions from several sources. The emissivity of the specular sea surface and atmosphere depend upon their physical compositions and thermodynamic state. Quantities that change relatively little, but do change, include SST and salinity, and the atmospheric temperature, pressure, and moisture.

To examine the sensitivity of wind speed estimates, a radiative transfer model, developed from Ulaby et al. (1986) is used, and these oceanic and atmospheric quantities are individually perturbed while holding all other quantities constant. The differences in the wind speed estimates from the solutions obtained, assuming the prescribed values are correct, are then generated for the range of wind speeds observed by the SFMR in hurricanes.

a. Sensitivity to oceanic variability

Wind speed errors due to variability in the specified SST (top) and the surface salinity (bottom) are shown in Fig. 10. The SST assumes a value of 28°C in the model. If the SST were overestimated by +1°C (i.e., the actual SST were 27°C), at a wind speed of $U_{10} = 20$ m s^{-1}, the wind speed would be in error by approximately $\Delta U_{10} = -0.5$ m s^{-1}, or the estimated wind speed would be 19.5 m s^{-1}. The physical reason behind this is that at nadir incidence angle there is a monotonic increase in T_B with SST. A cooler SST would therefore exhibit a lower apparent T_B, leading to a weaker surface wind estimate. The opposite is true for salinity, as T_B decreases with increasing salinity (Ulaby et al. 1986).

At speeds greater than 20 m s^{-1}, the wind speed errors are less than ±2 m s^{-1} for SST errors of ±3°C. Since in a typical hurricane ocean environment the SST varies less than this (Cione et al. 2000), these errors are tolerable when compared with the rmse associated with the GPS verification (~3.3 m s^{-1}). Similarly for the estimated salinities, the errors are generally less than 0.5 m s^{-1}, because the T_B sensitivity to changes in salinity is very small. Since the upper ocean is normally so well mixed that salinities vary by no more than 2%–3‰, these errors are insignificant.

b. Sensitivity to atmospheric variability

Knowledge of the composition of the intervening atmosphere presents a difficult challenge for sea surface remote sensing. Although in the absence of rain the atmosphere is nearly transparent, it still accounts for about 5% of the ocean's apparent T_B in the frequency band of interest. Changes in composition are significant throughout the hurricane environment, but the total columnar structure cannot be adequately sampled on a real-time basis. For this reason, a constant atmospheric structure is assumed during the course of a flight. Input to the radiative transfer model is the Jordan (1958) mean hurricane season West Indies sounding (temperature, pressure, and relative humidity as functions of altitude). Output is the atmospheric transmissivity at each of the operating frequencies of the SFMR, from which a linear dependence of transmissivity on frequency is approximated.

The assumed SFMR model relationship along with total gas (O_2 and H_2O_v) transmissivity values calculated from other atmospheric soundings that might be encountered during a mission are shown in the upper plot of Fig. 11. The lower plot shows the errors in wind speed that would occur given knowledge of atmospheric variability (dry air and water vapor) using well-documented atmospheric soundings. A mean profile is also computed from GPS soundings within 500 km of storm centers during the 1998 and 1999 HRD field programs.

In Fig. 11a, the increase in the spread of the transmissivity at higher frequencies is due to the water vapor absorption band near 22 GHz. In other words, drier atmospheres are more transparent at SFMR frequencies. Though extreme conditions such as the 45°N winter profile are not likely to be found in the Tropics, there is considerable variability in thermodynamic structure, especially as the aircraft transitions from the nearly saturated eyewall to the dry eye. This leads us to question how this might affect SFMR wind speed measurements.

The sensitivity to relative errors in the assumed atmospheric microwave transmission is shown in Fig. 11b. Physically a sounding with higher water vapor content (such as the eyewall) is less transparent (more absorptive) and therefore has a higher T_B at a given physical temperature, which would then lead to an overestimation of surface wind speed. The largest errors ($<\pm 1.5$ m s^{-1}) are still relatively small when compared to the overall error associated with the SFMR versus GPS comparison. Based

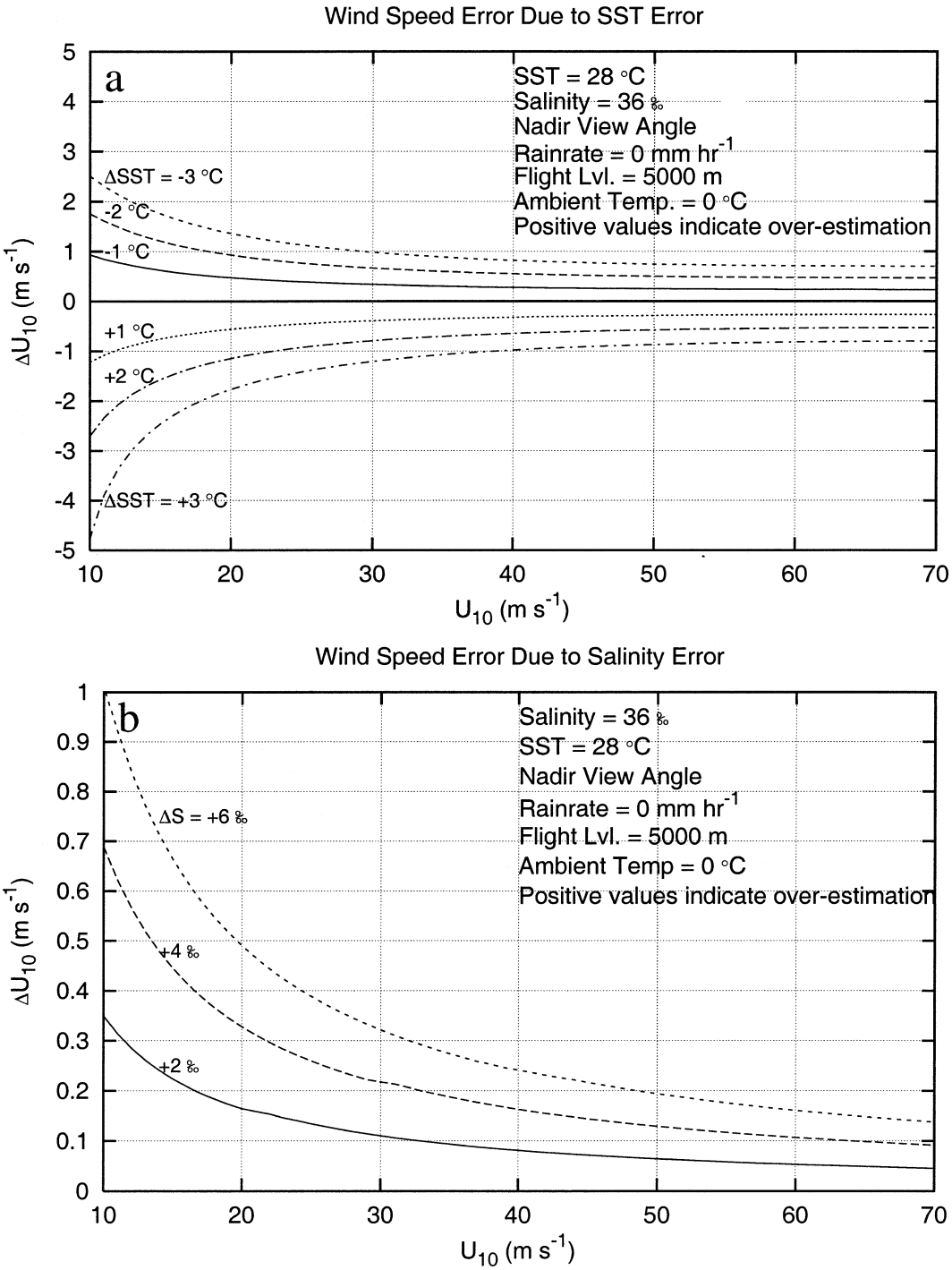

FIG. 10. Wind speed errors associated with incorrectly assumed SSTs (top) and salinities (bottom). For both plots the assumptions are SST = 28°C; S = 36‰; rain rate = 0 mm h^{-1}; flight level is 5000 m and the ambient atmospheric temperature is 0°C.

on these analyses we conclude that our assumptions concerning unknown variables in the microwave radiative transfer problem are of reasonable quality and that these variables will not contribute significantly to erroneous surface wind speed estimates.

c. Sensitivity to surface wind direction

Another possible source of error in the SFMR wind speed measurement is the effect of wind direction on the sea surface emissivity when viewed at nadir. The

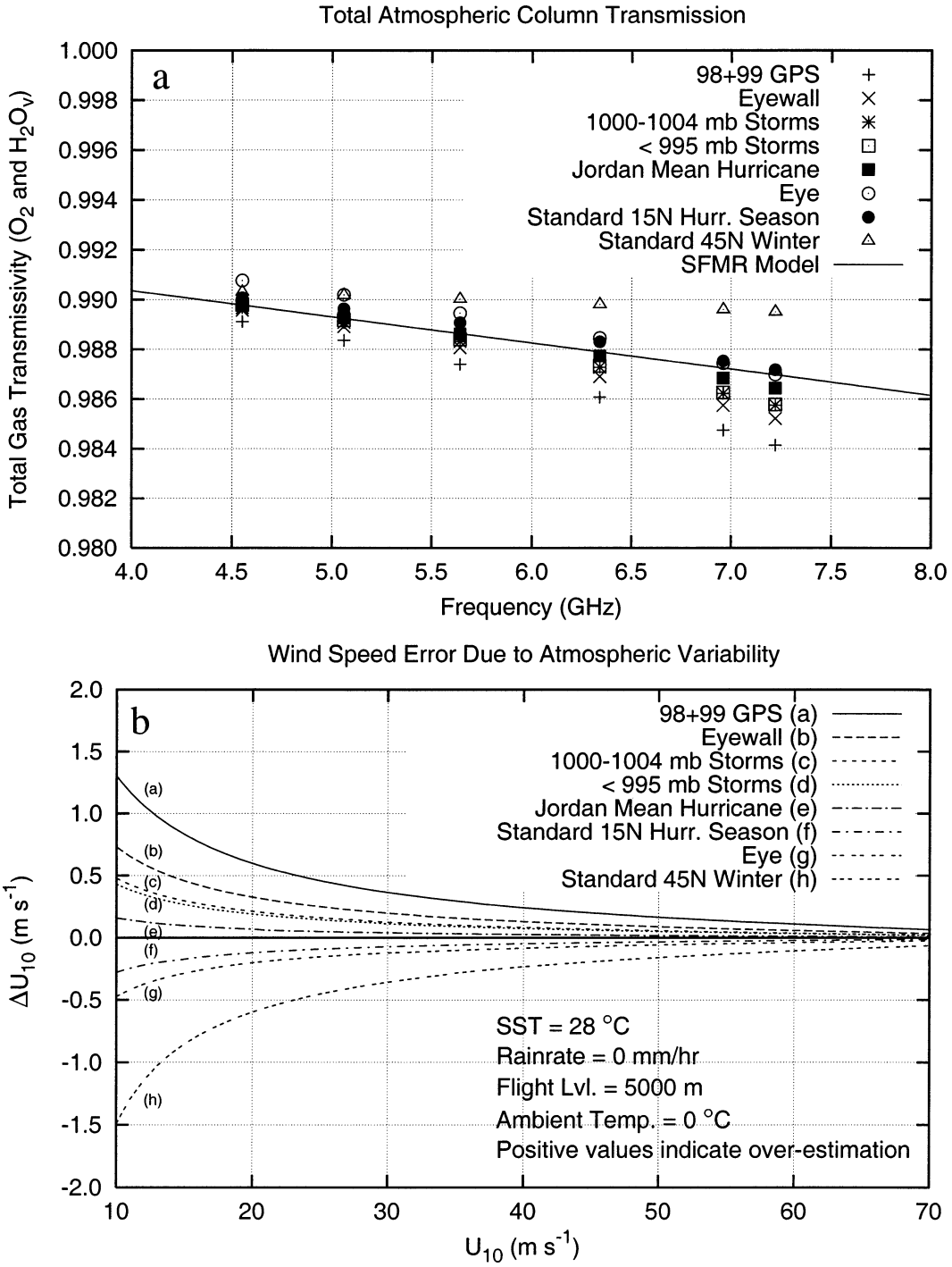

FIG. 11. Total one-way atmospheric transmission coefficient (τ_∞) as a function of frequency for several atmospheric soundings (a) and surface wind speed errors associated with incorrectly assumed atmospheric structure (b) based on two-way transmission ($\tau_\infty + \tau_{A/C}$). Assumed values are as in Fig. 10. See appendix A for notation explanation. The profiles used to compute the transmission are labeled as follows: 1000–1004 mb and <995 mb storms are from data compiled by Sheets (1969); eyewall data from Frank (1977); eye data from Jordan (1957); Jordan mean tropical data from Jordan (1958); *U.S. Standard Atmosphere* profiles for 15°N during hurricane season and for 45°N during winter (U.S. Government Printing Office 1976).

SFMR retrieval algorithm does not currently take this into account since the contribution of ocean surface roughness to the emissivity is assumed to be negligible at zero incidence. Previous studies (e.g., Tran et al. 2002) have documented a modulation of the wind-induced excess emissivity by the orientation between satellite radiometers and the local surface wind vector (i.e., the angular difference between antenna polarization direction and sea surface roughness elements). At wind speeds above 10 m s^{-1}, as much as a 10% difference between cross-wind and up-/downwind induced excess emissivity has been observed. We again question what effect, if any, this variability might have on surface wind speed retrievals.

Tran et al. (2002) indicate that at 18 GHz and nadir incidence, the wind direction modulation of excess emissivity has a maximum magnitude of $\sim 1.5 \times 10^{-3}$ that occurs at around 11.5 m s^{-1}, with a leveling off or a slight decrease at higher wind speeds. Assuming a negligible frequency dependence, this corresponds to a ΔT_B of around 0.5 K, for which it should be noted is near the level of the SFMR's inherent instrument noise (see appendix B). Applying this perturbation to the SFMR model gives a maximum error of $\sim \pm 1.5$ m s^{-1} between 10 and 15 m s^{-1}, where the wind direction–induced bias would be expected to be the greatest, which is in fact on the order of 10%. This error is less than the variability associated with the SFMR–GPS independent verification and, given the sparse data sample, likely could not be detected if the errors in the SFMR–GPS data were analyzed according to the observed surface wind direction.

5. Discussion

The SFMR infers sea surface wind speed from the increased T_B due to foam coverage, which is apparently a function of the local energy input from the wind, and perhaps the local wave environment. Thus the significant deviations found between remotely sensed and in situ winds can be attributed to generation of white water independent of the wind speed. For example, Webster et al. (1976) separately examined microwave T_B dependence on wind speed and fetch length. It was concluded that white water coverage increased with fetch, nearly independently of the surface wind speed. In fact, they found little dependence of T_B with fetch, but the C-band measurements were made at 38° off nadir and therefore small-scale roughness likely contributed to emission as short gravity–capillary waves increased with decreased fetch. Ross and Cardone (1974) found a relationship between whitecap coverage and fetch length, with an especially strong dependence for fetches shorter than 100 km. Additionally, the foam coverage was found to be related to whitecaps, suggesting the possibility of a T_B dependence on fetch.

In reality, the generation of white water is a result of breaking surface gravity waves. Several factors can contribute to the onset of small-scale wave breaking: direct energy input from the local wind, straining due to the orbital motion of longer wave components, and nonlinear transfers of energy from other wave components (Banner 1986). It is well known that the amount of wind energy input to surface waves is related to the ratio of wind speed to the wave phase speed, known as the inverse wave age (Donelan et al. 1993). The development of the surface wave field under hurricanes can be viewed as a highly complex example of fetch-limited wave growth, where peaks in observed wave energy spectra generally are shifted to lower frequencies as fetch increases.

Observations of directional wave spectra in the vicinity of hurricanes (Wright et al. 2001; Holt and Gonzalez 1986; King and Shemdin 1979; Elachi et al. 1977; Pore 1957) all reveal similar properties. Longer dominant waves that propagate faster than the storm speed exist in the forward quadrants. This is the region of extended fetch in which seas have developed further, that is, the peak of the wave energy spectrum has shifted to lower frequencies. The dominant waves in the forward quadrants generally propagate to the right of the local wind. The RR quadrant contains dominant waves of shorter wavelength with slower phase speeds, and for a moving storm is the location where the local wind vector is more or less aligned with the direction of surface wave propagation. Therefore, it is the region of active wave generation, characterized by limited fetch and therefore high wind speed to phase speed ratio. It is speculated that in this fetch-limited area the white water coverage is reduced since the seas are still in a building stage; thus the assumption that the foam (and microwave emission) is dependent only on the local wind speed will lead to an underestimate of the wind. In the LR quadrant the situation is more complicated since the wind vector can *oppose* the dominant wave direction, leading to an actively building high-frequency, wind-dominated sea coexistent with a decaying swell field. In reality, multimodal spectra are observed in all regions of hurricanes (Wright et al. 2001; Harris 1986), so the nonlinear interaction of components complicates the process beyond this simple discussion. Nevertheless, it appears that the SFMR is not only capable of real-time diagnosis of high surface winds, but that much of the error in the wind estimates may well be related to sea state.

Qualitative assessment of the vertical structure of hurricanes is possible by combining measurements of the SFMR surface wind with flight-level wind data. A cross section of the wind speed and rain rate plotted as function of r/r_0 from Hurricane Georges (1998) is shown in Fig. 12a and the corresponding T_B are plotted in Fig. 12b. The conical shape of the eyewall as observed by airborne radar and documented by Marks et al. (1992), and more recently quantified from GPS sonde measurements by DLH, is seen in the inward displacement surface wind maximum relative to flight level. The ef-

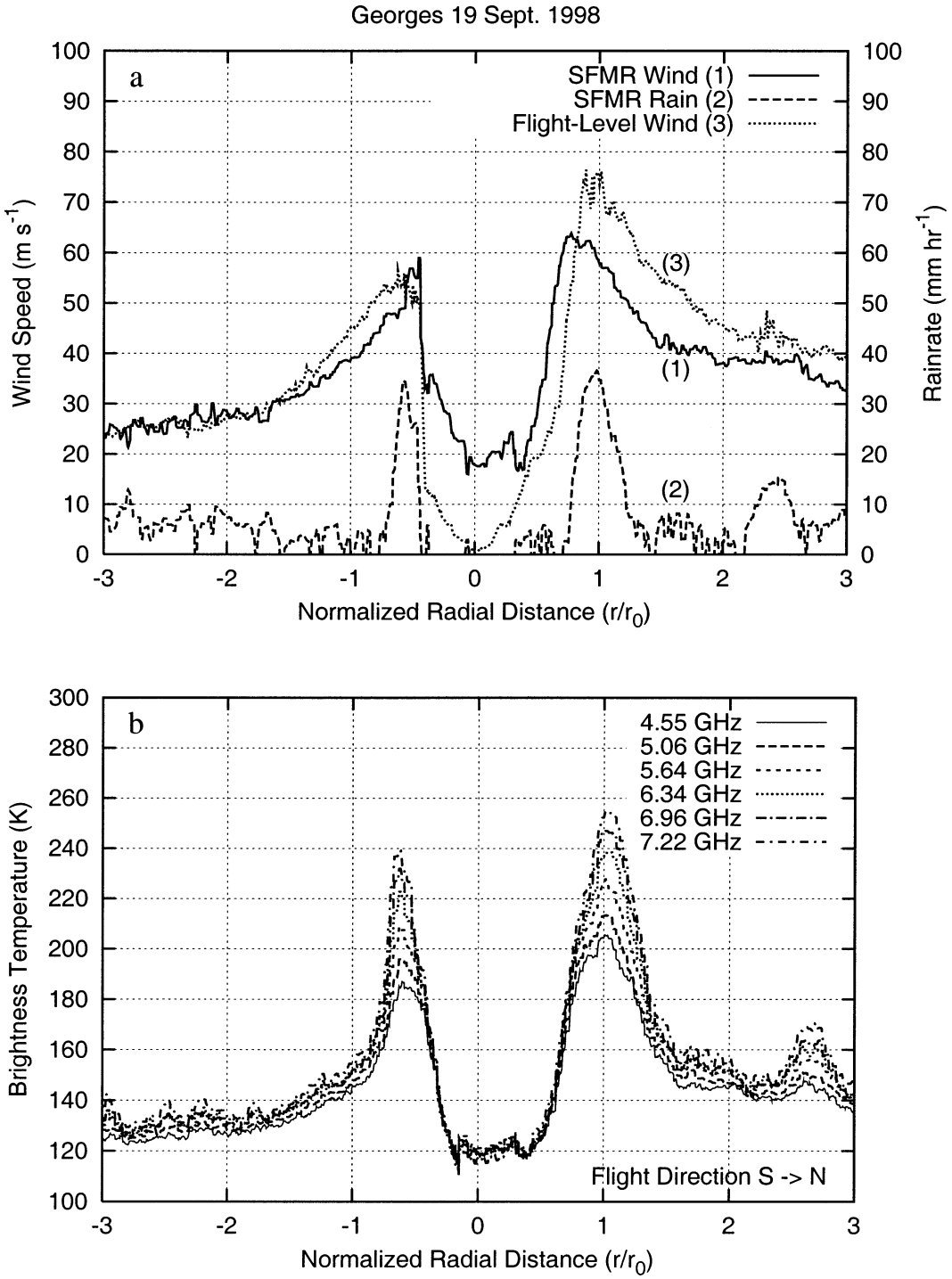

FIG. 12. (a) SFMR and flight-level wind speeds (m s^{-1}) and SFMR rain rate (mm h^{-1}) and (b) T_B as a function of normalized radial distance (r/r_0) from the center of Hurricane Georges, where $r_0 = 27$ km is defined by the flight-level wind maximum in the north eyewall. Flight direction is south (left) to north (right). In (b), T_B generally increases with higher frequency.

fects of environmental shear on the storm are seen by both the weak correlation between the flight-level and surface asymmetries, and the south-to-north tilting with height of the vortex. Supplemented with a perpendicular cross section of surface and flight-level measurements, the environmental shear vector can be unambiguously deduced. An additional observation is the relationship between the wind measurements and the SFMR rain

rate. The rain-rate maximum is aligned vertically with the flight-level wind (and convection) maximum and decreases to near zero at the SFMR surface wind maximum. Thus the rain-rate measurement is not responding merely to the increase in T_B but to actual rainfall absorption effects.

A commonly observed phenomenon, as illustrated in Fig. 12a, is that the SFMR continues to retrieve surface winds within the eye of hurricanes, where it is expected that winds normally decrease below 10 m s^{-1}. One previous hypothesis of this systematic overestimate was due to the hurricane's warm core increasing the observed T_B. Based on the sensitivity analysis in section 4, this is clearly not the cause as the drier and less dense (albeit thermometrically warmer) air inside the eye exhibits a lower T_B and therefore an *underestimate* of wind would occur. The overestimate is probably a result of either the misalignment of the flight-level and surface vortex centers, or, more likely, the time lag between the slackening wind and the decay of the sea state.

6. Conclusions

Passive microwave radiometry is a useful tool for measurement of sea surface and atmospheric properties. Additionally, measurements at nadir incidence and lower frequencies (i.e., $<$10 GHz) do not suffer from severe rainfall attenuation and, unlike many active radar systems, do not become saturated at hurricane-force wind speeds. Moreover, surface wind speeds in hurricanes derived from measurement of microwave emissions from the wind-driven sea surface are well correlated with in situ surface wind measurements by GPS dropwindsonde. The SFMR provides independent estimates of surface winds at a horizontal resolution of $\sim$10 s (1.5 km) along the flight track, suitable for correct location and estimation of maximum sustained wind speeds, as well as high-resolution mapping of the wind field. Currently the SFMR is the only reliable passive microwave instrument for measuring surface winds $>$20 m s^{-1}, as measurements from spaceborne platforms have not been validated in this range.

The overall high bias of the SFMR wind estimates relative to the 10-m GPS winds may be due to differences in the timescales of motion represented by each of the measurements. The GPS surface wind is estimated from an average wind speed across the atmospheric boundary layer and therefore may not contain as much ''gustiness,'' or intermittent variability, measured by the SFMR averaged over a shorter time period. The SFMR may in the future provide a guide to assess the statistical variability of the GPS measurements, which to date is not well understood.

Errors induced by incorrect estimation of unknown variables in the radiative transfer problem are tolerable. The assumed values require, at most, minor adjustment from their present values. It appears that the sea state has an influence on the retrieved wind speeds, as revealed by the significant differences in SFMR–GPS biases among storm quadrants. The RR quadrant of storms is where the wind vector is generally aligned with the direction of dominant wave propagation. Thus waves are in an active building state and because they may not produce the large foam patches in their wake after breaking, the wind speed is underestimated relative to the other storm quadrants.

Breaking waves play an important part in the transfers of enthalpy and momentum at the air–sea interface (Longuet-Higgins 1986). Sea spray generated by breaking waves may be important for the large source of sensible and latent heat to hurricanes (Andreas and Emanuel 2001). Breaking waves are also the primary source of momentum to the upper ocean (Craig and Banner 1994), which, through a number of processes such as vertical shear, entrainment, and advection, acts to significantly redistribute heat that necessarily feeds back to the hurricane (Jacob et al. 2000). We hope that in the near future we will be able to better determine the relationship between passive microwave measurements of the sea surface and the air/sea fluxes that partly govern the intensity change process in tropical cyclones.

Acknowledgments. The authors acknowledge the conceptual insight of Prof. Calvin T. Swift, University of Massachusetts Microwave Remote Sensing Laboratory (MIRSL), for development of the original SFMR at the NASA Langley Research Center. Subsequent design and fabrication of a second generation SFMR was carried out at MIRSL under the supervision of Prof. Swift and Prof. Robert McIntosh, founding director of MIRSL. Much of the original SFMR design, antenna development, and testing as well as system calibration was performed at MIRSL by Dr. Al Tanner (currently NASA/JPL) and Dr. Mark Goodberlet (currently ProSensing, Inc., formerly Quadrant Engineering). Dr. Christopher Ruf (currently University of Michigan) developed the retrieval algorithm for wind speed and rain rate. Dr. Karen St. Germain (currently NRL/Washington) improved the instrument design and assisted in the data analysis and development of the retrieval algorithm.

The Office of the Federal Coordinator for Meteorology (OFCM) provided funding for development of the operational third-generation SFMR currently flown on the NOAA WP-3D. We especially thank Robert Dumont, OFCM, for his continued support of the SFMR concept.

We wish to express our sincere gratitude for the support and dedication of the NOAA Aircraft Operations Center. The integration of the SFMR system would have been impossible without the assistance of the engineers and flight crew at AOC. Dr. James McFadden, AOC hurricane program manager, coordinated the many requests for flight support during the hurricane seasons.

We also thank the many colleagues at HRD who supported the SFMR program, especially Dr. Hugh Willoughby, Director, and Dr. Frank Marks, Field Program

Director. We thank Dr. Mark Powell for his effort to incorporate SFMR data into the HRD real-time surface wind analysis (H*WIND), and William Barry for development of the SFMR display application.

The support and feedback from our colleagues at the National Hurricane Center has been crucial to improvement of the SFMR. We especially acknowledge NHC Director Max Mayfield, Miles Lawrence, Dr. Richard Pasch, and James Franklin. Finally we thank Dr. Chris Landsea, John Kaplan, Dr. Hugh Willoughby (HRD), Dr. Lynn Shay (UM/RSMAS), and three anonymous reviewers who all contributed significantly to the improvement of the manuscript.

APPENDIX A

SFMR Algorithm

a. Forward radiative transfer model

The SFMR infers the ocean surface wind speed from thermal blackbody radiation emitted by the sea, governed by Planck's law. Additionally, the Rayleigh–Jeans approximation to Planck's law (applicable at microwave frequencies) implies a linear relationship between the radiated energy, expressed in terms of a brightness temperature (T_B), and physical temperature T. Materials such as the atmosphere and sea surface emit a portion of absorbed energy; this ratio is the emissivity

$$\varepsilon = \frac{T_B}{T}. \tag{A1}$$

From Kirchoff's energy conservation law, the emission and absorption of energy by a material in local thermodynamic equilibrium must be equal. Since the radiation not emitted by a medium must (neglecting scattering effects) be transmitted,

$$\varepsilon = 1 - \tau, \tag{A2}$$

where τ is the transmissivity.

As shown in Fig. A1, the apparent brightness temperature T_B of the sea surface measured by a downward-looking radiometer positioned at some height above the surface is the sum of several sources (e.g., Ulaby et al. 1981):

1) cosmic radiation attenuated by the atmosphere and reflected by the surface (T_{COS}),
2) downward emission by the atmosphere reflected by the surface (T_{DOWN}),
3) emission from the surface attenuated by the intervening atmosphere (T_{OCEAN}), and
4) upward emission from the intervening atmosphere (T_{UP}).

The absorption, emission, and transmission properties of the atmosphere are mainly due to

1) absorption by oxygen molecules,
2) absorption by water vapor molecules, and

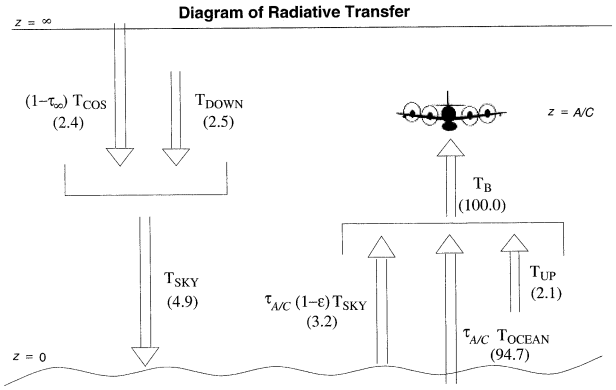

FIG. A1. Diagram depicting radiative contributions to total brightness temperature measured by a nadir viewing radiometer. The emissivity ε is the quantity directly related to the surface wind speed. The quantities in parentheses below each term indicate contributed units ($\times$ 100%) to the total apparent brightness temperature. Values are for the ocean and atmosphere conditions assumed in the SFMR algorithm, zero wind and rain rate, at 5 GHz. For reference $T_B \simeq 114.0$ K.

3) absorption and scattering by liquid water particles.

The atmospheric contribution T_{DOWN} to the apparent brightness temperature is considered to be the sum of gaseous and hydrometeor contributions:

$$T_{\mathrm{DOWN}} = (1 - \tau_{r,\infty})\langle T_{r,\infty}\rangle + \tau_{r,\infty}(1 - \tau_{a,\infty})\langle T_{a,\infty}\rangle, \tag{A3}$$

where T is the physical temperature (K); the subscripts r and a refer to rain and atmospheric transmission, respectively; ∞ indicates contribution by the total atmospheric column; and the angle brackets denote a mass-weighted layer average. The total sky brightness temperature is then just the sum of T_{DOWN} and the extraterrestrial source ($T_{\mathrm{COS}} = 2.7$ K):

$$T_{\mathrm{SKY}} = T_{\mathrm{DOWN}} + (1 - \tau_{r,\infty}\tau_{a,\infty})T_{\mathrm{COS}}. \tag{A4}$$

The true ocean brightness temperature is related to the SST by $T_{\mathrm{OCEAN}} = \varepsilon(\mathrm{SST})$. Since it is directly related to the wind speed, the calculation of ε is the goal of the SFMR algorithm. The ocean contribution is added to the reflected sky brightness temperature, $(1 - \varepsilon)T_{\mathrm{SKY}}$, which is then attenuated by the intervening atmospheric layer below the aircraft. The upward emission by the atmosphere below the aircraft is

$$T_{\mathrm{UP}} = (1 - \tau_{r,A/C}\tau_{a,A/C})\langle T_{a,A/C}\rangle, \tag{A5}$$

where A/C indicates emission from the atmospheric layer below the aircraft. The total apparent brightness temperature of the ocean surface is then just the sum

$$T_B = (\tau_{r,A/C})(\tau_{a,A/C})[T_{\mathrm{OCEAN}} + (1 - \varepsilon)T_{\mathrm{SKY}}] + T_{\mathrm{UP}}. \tag{A6}$$

Under calm winds, typical tropical (rain free) atmospheric conditions, and nominal flight altitudes the contribution by T_{OCEAN} represents ~95% of the total apparent brightness temperature of the ocean. The calculation of transmissivity from the atmospheric com-

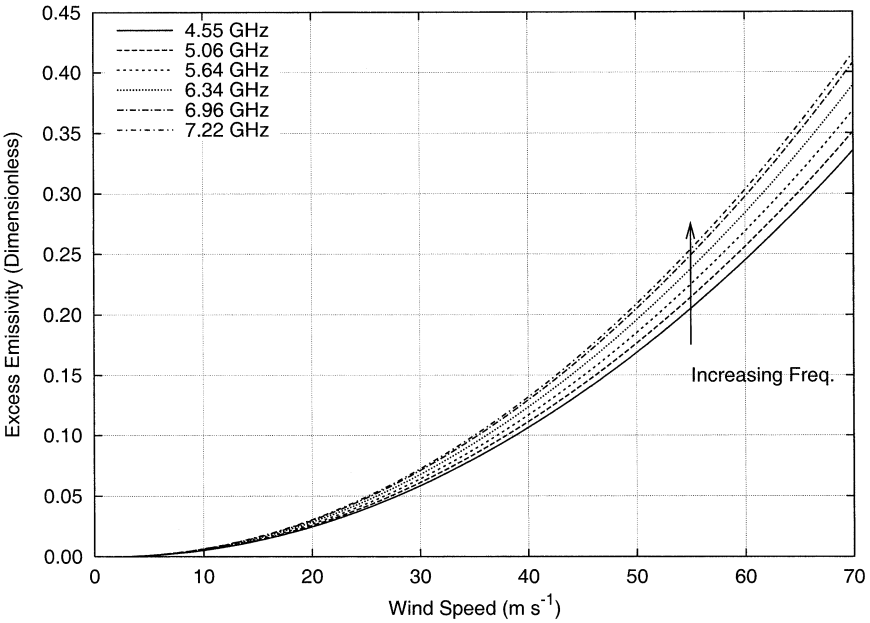

FIG. A2. Excess emissivity (dimensionless) as a function of wind speed (m s^{-1}). The specular emissivity for typical ocean conditions is ~0.35.

position is given in Ulaby et al. (1986). For real-time application of the algorithm the thermodynamic properties of the atmosphere assume tropical characteristics (Jordan 1958).

b. Emissivity–wind speed relationship

The ocean absorbs only a portion of the incident radiation. The remainder of the incident energy is reflected, and therefore the relationship between emissivity and reflectivity is just $\varepsilon = 1 - \Gamma$. Expressed in functional form the reflectivity of a smooth (specular) ocean surface is

$$\Gamma_p = \Gamma_p(\theta, f, \text{SST}, S), \tag{A7}$$

where p is the polarization state (vertical or horizontal), θ is incidence angle, f is electromagnetic frequency, SST is sea surface temperature, and S is the salinity. Since SFMR measurements are normally made at zero incidence angle where the reflectivity is independent of the polarization, the subscript p may be dropped. The reflectivity is then calculated at each of the SFMR frequencies assuming the SST and salinity are known.

As the wind begins to transfer energy to the ocean, the scattering and emission properties become much more complicated. As the wind stress increases, the sea surface becomes roughened by capillary and short gravity waves, which break when they reach a critical steepness. This breaking produces layers of foam patches and streaks that emit microwave energy more readily than does a specular surface. So-called foam models have been developed that relate the fractional coverage of foam to the wind speed (Ross and Cardone 1974; Tinga et al. 1973; Stogryn 1972). The SFMR algorithm assumes the total emissivity of the ocean surface consists of wind speed–dependent components and specular components.

The relationship between the emissivity and hurricane-force winds (Black and Swift 1984) was established through dual aircraft missions in which brightness temperature measurements were made by one aircraft operating at around 3-km altitude, compared with lower flying aircraft making in situ measurements of winds at between 0.5- and 1.5-km altitude, and reduced to near-surface values using the boundary layer model of Powell (1980). The emissivity of the wind-driven sea was then determined by estimation of the increase relative to a specular sea surface. The specular Fresnel power reflection coefficient (Γ) is calculated using the algorithm of Klein and Swift (1977), which immediately gives the smooth surface emissivity. This is then added to the wind-generated excess (Fig. A2) to obtain the total emissivity.

What remains to be determined is the emissivity of the rain column. Solving Eq. (A6) for ε gives

$$\varepsilon = \frac{a\tau_{r,\infty} - b}{a\tau_{r,\infty} - c\tau_{r,A/C}}, \tag{A8}$$

where

$$a = \frac{(\langle T_{a,\infty}\rangle - T_{\text{COS}})\tau_{a,\infty}}{\langle T_{a,\infty}\rangle}, \qquad b = \frac{\langle T_{r,\infty}\rangle - T_B}{\langle T_{a,\infty}\rangle},$$

$$c = \frac{\langle T_{r,A/C}\rangle - \text{SST}}{\langle T_{a,\infty}\rangle}.$$

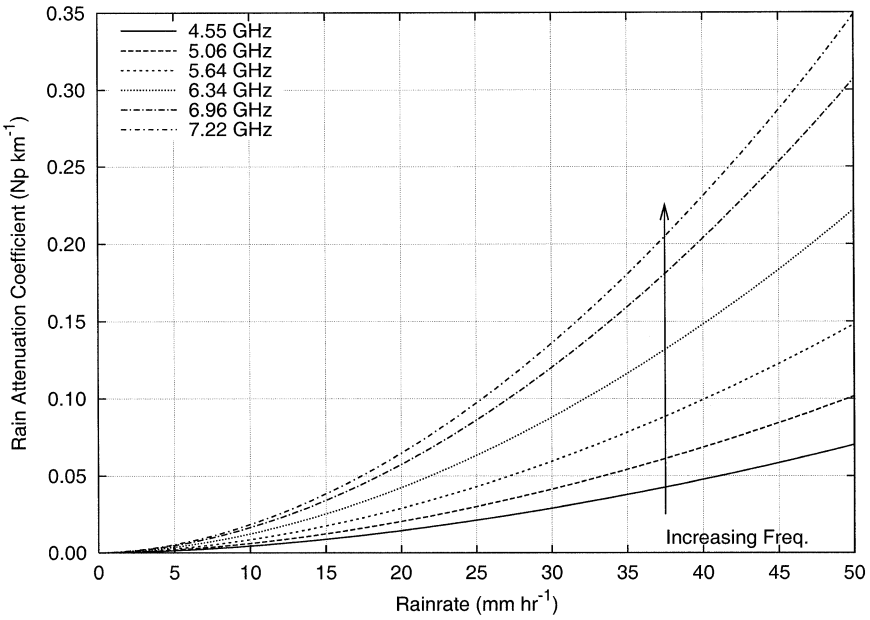

FIG. A3. Rainfall attenuation coefficient κ_r (Np km^{-1}) plotted as a function of rain rate (mm h^{-1}). The differential absorption (i.e., the spread of κ_r) of microwave radiation determines the rain rate.

By neglecting ($\langle T_{r,A/C}\rangle$ − SST) and T_{COS} in comparison to $\langle T_{a,\infty}\rangle$, $a = \tau_{a,\infty}$, $c = 0$, an approximate expression for the emissivity of the sea surface in the presence of rain results:

$$\varepsilon \approx \left[\frac{T_B - \langle T_{r,\infty}\rangle}{\langle T_{a,\infty}\rangle}\right]\frac{1}{\tau_{a,\infty}\tau_{r,\infty}^2} + 1. \tag{A9}$$

Because of the small ratio of raindrop size to the SFMR electromagnetic wavelength, scattering is negligible, even at the high rain rates experienced in hurricanes. Thus rain can be approximated entirely by an absorption process. The transmissivity of the rain column depends upon hyrdometeor content, which is proportional to rain rate, and electromagnetic frequency. The relationship between transmissivity and absorption, κ_r, is

$$\tau_r = \exp(-\kappa_r h), \tag{A10}$$

where h is the depth of the rain column. The rainfall absorption coefficient is modeled by

$$\kappa_r = aR^b, \tag{A11}$$

where R is the rain rate (mm h^{-1}) and a, b have been empirically determined. Olsen et al. (1978) have shown that a is a function of rain rate and frequency:

$$a = gf^{n(R)}. \tag{A12}$$

Atlas and Ulbrich (1977) indicate that $n \approx 2.6R^{0.0736}$. The exponent $b = 1.35$ has been determined from C-band radar reflectivity measurements in hurricanes by Jorgensen and Willis (1982). The calibration studies of Black and Swift (1984) arrived at a value of $g = 1.87 \times 10^{-6}$ Np km^{-1}. The rainfall attenuation coefficient [Eq. (A11)] is plotted as a function of rain rate in Fig. A3. Nominally rain rates > 5 mm h^{-1} can be measured by the SFMR. As was shown in Fig. 12b in section 5, the absorptive effect of rain can be seen in the increase of the spread of T_B in the eyewall.

c. Inversion algorithm

The SFMR thus measures the apparent T_B of a scene below the aircraft that results from contributions from both the ocean and the atmosphere. For a given SST, the change in emissivity is directly related to T_B. In addition, the frequency dependence of microwave attenuation by rainfall can be used to infer the quantity of liquid precipitation in the atmospheric column below the aircraft. Retrieval of the surface wind speed and rain rate from a set of measurements of T_B constitutes an inverse problem that generally requires the number of measurements to be greater than or equal to the number of parameters retrieved. For the case of the SFMR where six measurements are used to infer two parameters (wind speed and rain rate), the solution is overdetermined and a least squares inversion method is applied.

A physical model is designed that relates an n-length measurement vector of brightness temperatures $\mathbf{T}$ to an m-length vector of retrieved parameters $\mathbf{p}$ (Pedersen 1990):

$$\mathbf{T}_n = \mathbf{W}_{nm} \cdot \mathbf{p}_m, \tag{A13}$$

where the matrix $\mathbf{W}$ consists of the partial derivatives of $\mathbf{T}$ with respect to $\mathbf{p}$:

TABLE B1. Rms noise levels (ΔT_B, K) obtained from separate flights for the years analyzed in the article. These values should be compared with the theoretical 0.4-K noise level associated with 0.7-s integration time.

Frequency (GHz)	4.55	5.06	5.64	6.34	6.36	7.22
1998 (Georges 19 Sep) ΔT_B (K)	1.1	0.5	0.6	0.7	0.8	0.9
1999 (Floyd 14 Sep) ΔT_B (K)	0.9	0.5	0.7	0.7	0.8	0.9
2001 (Humberto 24 Sep) ΔT_B (K)	1.2	0.5	0.6	0.6	0.9	1.0

$$\mathbf{W}_{nm} = \frac{\partial \mathbf{T}_n}{\partial \mathbf{p}_m}. \tag{A14}$$

A set of radiometer observations is denoted by

$$\hat{\mathbf{T}}_n = \mathbf{W}_{nm} \cdot \mathbf{p}_m + \boldsymbol{\epsilon}_n = \mathbf{T}_n + \boldsymbol{\epsilon}_n, \tag{A15}$$

where $\boldsymbol{\epsilon}_n$ is an error vector, and the top hat indicates an estimate of the true parameter. The solution vector of parameter estimates is computed from

$$\hat{\mathbf{p}} = (\mathbf{W}^{\mathrm{T}}\,\mathbf{W})^{-1}\,\mathbf{W}^{\mathrm{T}}\,\hat{\mathbf{T}}, \tag{A16}$$

obtained from the condition that the sum of squared differences between the observed and model-predicted brightness temperatures is minimized, that is,

$$\sum_{i=1}^{n}\left[\hat{\mathbf{T}}_i - \sum_{j=1}^{m}\mathbf{W}_{ij}\hat{\mathbf{p}}_j\right]^2 = \text{minimum}. \tag{A17}$$

Solutions to the problem are possible when the derivative matrix elements $\mathbf{W}_{ij}$ are significantly different from one another so that the elements of $(\mathbf{W}^{\mathrm{T}}\mathbf{W})^{-1}$ do not spuriously amplify the errors $\boldsymbol{\epsilon}_i$. For wind speeds <10 m s^{-1} or rain rates <5 mm h^{-1}, the sensitivity of changes in the T_B to changes in these quantities at SFMR frequencies and nadir incidence angle is so weak that a solution is normally not possible.

APPENDIX B

System Specifications, Calibration, and Noise Figures

The SFMR measures the apparent T_B at six microwave frequencies (4.55, 5.06, 5.64, 6.34, 6.96, 7.22 GHz) over 200-MHz bandwidths. The hardware averaging time is set at 0.7 s, which gives a theoretical single-measurement brightness temperature resolution (noise) of $\Delta T_B = 0.4$ K. The brightness temperatures are collected sequentially from the six channels, so it should take $6 \times 0.7 = 4.2$ s to collect a complete set of data. However, the system analog-to-digital converter samples at a slightly faster rate, so a complete set of data is obtained approximately every 3.5 s. The response time of the instrument is 0.85 s per channel, which is slightly higher than the averaging time of 0.7 s since the onboard processor does not spend the entire time collecting data. The time between independent sets of measurements is generally defined as twice the response time of the system, so the actual time between completely independent sets of data is 2×6 channels $\times$ 0.85 s per channel $= 10$ s (Goodberlet and Swift 1996). At a typical aircraft ground speed of 150 m s^{-1}, this corresponds to a spatial resolution of 1.5 km along the flight track. Additionally, the size of the footprint on the ocean surface depends upon the flight altitude, the physical dimensions of the antenna, and the microwave frequency. The half-power (-3 db) main beamwidth ranges from 22° to 32°, so at a typical flight altitude of 1500 m, the cross-track footprint has a diameter of between 600 and 800 m, depending upon the channel.

Calibration of the SFMR requires relating the output receiver voltage to T_B at each channel. For a balanced Dicke-switched noise-injection type radiometer (Ulaby et al. 1981), the T_B at a particular frequency depends upon the the reference load (T_{REF}) and noise diode (T_{NSD}) physical temperatures as well as the sensor's output voltage, V (Goodberlet and Swift 1996). The SFMR is designed to hold T_{REF} and T_{NSD} near a constant value of 313 K (40°C), which improves the stability of the calibration. The sensor T_B (K) is then related to the output voltage via the linear regression equation

$$T_B = (a + bT_{\mathrm{NSD}})V + cT_{\mathrm{REF}} + d. \tag{B1}$$

Measurements of T_B are made by observing known cold (clear sky $\sim$ 5 K), warm blackbody absorber (liquid N_2 $\sim$ 77 K), and hot (ground surface) targets. The calibration regression is improved by making measurements over the ocean at known SST and light wind speed and using the Klein–Swift algorithm to compute the specular sea surface T_B.

The SFMR's system noise may be estimated by calculating the distribution of random fluctuations about running mean values of T_B of the observed calm sea surface under clear-sky conditions. To analyze the inherent instrument noise contained in the 1998, 1999, and 2001 SFMR data, we chose a 10-min continuous run of low T_B from each year. The rmse about the 1-min running mean values for each channel is computed. The data are chosen to be truly representative of quiescent wind and sea state far from the center of their respective storms. Additionally, the data are void of RFI contamination. Table B1 shows the noise levels of the brightness temperatures for each channel.

The ΔT_B values stated in Table B1 are for the 1-Hz data and should be compared with the theoretical noise of 0.4 K (based on the 0.7-s instrument integration time). The noise levels may be reduced further by time averaging the digital data, at the expense of resolution. It is obvious, based on these results, that the SFMR receiver and antenna noise is quite low and should not contribute significantly to errors when the derived wind

speeds are compared to the dropsonde surface winds. Additionally, an encouraging result is the stability of the noise levels from year to year. No recalibration was performed between 1998 and 1999, and the noise is essentially unchanged. The recalibration prior to the 2001 season produced comparable results.

REFERENCES

Andreas, E. L., and K. A. Emanuel, 2001: Effects of sea spray on tropical cyclone intensity. *J. Atmos. Sci.,* **58,** 3741–3751.

Atlas, D., and C. W. Ulbrich, 1977: Path- and area-integrated rainfall measurement by microwave attenuation in the 1–3 cm band. *J. Appl. Meteor.,* **16,** 1322–1331.

Banner, M. L., 1986: A comparison of the wave-induced momentum flux to breaking and nonbreaking waves. *Wave Dynamics and Radio Probing of the Ocean Surface,* O. M. Phillips and K. Hasselmann, Eds., Plenum Press, 321–333.

Barrick, D. E., and C. T. Swift, 1980: The Seasat microwave instruments in historical perspective. *IEEE J. Oceanic Eng.,* **OE-5,** 74–79.

Black, P. G., and W. L. Adams, 1983: Guidance for estimating surface winds based on sea state observations from aircraft and sea state catalog. NOAA Tech. Memo. FCM-G1-1983, 83 pp.

——, and C. T. Swift, 1984: Airborne stepped frequency microwave radiometer measurements of rainfall rate and surface wind speed in hurricanes. Preprints, *Second Conf. on Radar Meteorology,* Zurich, Switzerland, Amer. Meteor. Soc., 433–438.

Cione, J. J., P. G. Black, and S. H. Houston, 2000: Surface observations in the hurricane environment. *Mon. Wea. Rev.,* **128,** 1550–1561.

Craig, P. D., and M. L. Banner, 1994: Modeling wave-enhanced turbulence in the ocean surface layer. *J. Phys. Oceanogr.,* **24,** 2546–2559.

Delnore, V. E., G. S. Bahn, W. L. Grantham, R. F. Harrington, and W. L. Jones, 1985: Active and passive measurements in Hurricane Allen. NASA Tech. Rep. TM-86390, 138 pp.

Donelan, M., M. Skafel, H. Graber, P. Liu, D. Schwab, and S. Venkatesh, 1993: On the growth of wind-generated waves. *Atmos.–Ocean,* **30,** 457–478.

Dvorak, V. F., 1984: Tropical cyclone intensity analysis using satellite data. NOAA Tech. Memo. NESDIS-11, 47 pp.

Elachi, C., T. W. Thompson, and D. King, 1977: Ocean wave patterns under Hurricane Gloria: Observation with an airborne synthetic-aperture radar. *Science,* **198,** 609–610.

Frank, W. M., 1977: Structure and energetics of the tropical cyclone. Part I: Storm structure. *Mon. Wea. Rev.,* **105,** 1119–1135.

Goodberlet, M., and C. T. Swift, 1996: Development of a second generation stepped frequency microwave radiometer for IWRS. Tech. Rep. Prosensing, Inc. (formerly Quadrant Engineering), Amherst, MA, 42 pp.

Harrington, R. F., 1980: The development of a stepped frequency microwave radiometer and its application to remote sensing of the earth. NASA Tech. Rep. TM-81847, 169 pp.

Harris, D. L., 1986: Models for the hurricane wave field. *Wave Dynamics and Radio Probing of the Ocean Surface,* O. M. Phillips and K. Hasselmann, Eds., Plenum Press, 677–681.

Hock, T. F., and J. L. Franklin, 1999: The NCAR GPS dropwindsonde. *Bull. Amer. Meteor. Soc.,* **80,** 407–420.

Holt, B., and F. I. Gonzalez, 1986: SIR-B observations of dominant ocean waves near Hurricane Josephine. *J. Geophys. Res.,* **91,** 8595–8598.

Jacob, S. D., L. K. Shay, A. J. Mariano, and P. G. Black, 2000: The 3D oceanic mixed layer response to Hurricane Gilbert. *J. Phys. Oceanogr.,* **30,** 1407–1429.

Jarvinen, B. R., C. J. Neumann, and M. A. S. Davis, 1984: A tropical cyclone data tape for the North Atlantic basin, 1886–1983: Contents, limitations, and uses. NOAA Tech. Memo. NWS NHC-22, 21 pp.

Jones, W. L., P. G. Black, V. E. Delnore, and C. T. Swift, 1981: Airborne microwave remote-sensing measurements of Hurricane Allen. *Science,* **214,** 274–280.

Jordan, C. L., 1957: Mean soundings for the hurricane eye. National Hurricane Research Project Rep. 13, U. S. Weather Bureau, 10 pp.

——, 1958: Mean soundings for the West Indies area. *J. Meteor.,* **15,** 91–92.

Jorgensen, D. P., and P. L. Willis, 1982: A *Z–R* relationship for hurricanes. *J. Appl. Meteor.,* **21,** 356–366.

King, D. B., and O. H. Shemdin, 1979: Radar observations of hurricane wave directions. *Proc. 16th Int. Conf. Coastal Eng.,* Hamburg, Germany, ASCE, 209–226.

Klein, L. A., and C. T. Swift, 1977: An improved model for the dialectric constant of sea water at microwave frequencies. *IEEE J. Oceanic Eng.,* **OE-2,** 104–111.

Kraft, R. H., 1961: The hurricane's central pressure and highest wind. *Mar. Wea. Log,* **5,** 157.

Longuet-Higgins, M. S., 1986: Advances in breaking-wave dynamics. *Wave Dynamics and Radio Probing of the Ocean Surface,* O. M. Phillips and K. Hasselmann, Eds., Plenum Press, 209–230.

Marks, F. D., R. A. House Jr., and J. F. Gamache, 1992: Dual-aircraft investigation of the inner core of Hurricane Norbert. Part I: Kinematic structure. *J. Atmos. Sci.,* **49,** 919–942.

Martsinkevich, L. M., and V. V. Melent'ev, 1982: Relationship between microwave brightness temperature of a wind-driven sea and characteristics of the sea state and wave-forming factors (option-b). *USSR/USA Bering Sea Experiment,* K. Y. Kondrat'ev, Ed., Oxonian Press, 119–142.

Miller, B. I., 1958: The three-dimensional wind structure around a tropical cyclone. National Hurricane Research Project Rep. 15, U. S. Weather Bureau, 41 pp.

Nordberg, W., J. Conaway, and P. Thaddeus, 1969: Microwave observations of the sea state from aircraft. *Quart. J. Roy. Meteor. Soc.,* **95,** 408–413.

Olsen, R. L., D. V. Rogers, and D. B. Hodge, 1978: The aR^b relation in the calculation of rain attenuation. *IEEE Trans. Antennas Propagat.,* **AP-26,** 318–329.

Pedersen, L. T., 1990: Microwave radiometers. *Microwave Remote Sensing for Oceanographic and Marine Weather-Forecast Models,* R. A. Vaughn, Ed., Kluwer Academic, 177–190.

Pore, A., 1957: Ocean surface waves produced by some recent hurricanes. *Mon. Wea. Rev.,* **85,** 385–392.

Powell, M. D., 1980: Evaluations of diagnostic marine boundary layer models applied to hurricanes. *Mon. Wea. Rev.,* **108,** 757–766.

——, S. H. Houston, and T. A. Reinhold, 1996: Hurricane Andrew's landfall in South Florida. Part I: Standardizing measurements for documentation of surface wind fields. *Wea. Forecasting,* **11,** 304–328.

Rosenkranz, P. W., and D. H. Staelin, 1972: Microwave emissivity of sea foam and its effect on nadir radiometric measurements. *J. Geophys. Res.,* **77,** 6528–6538.

Ross, C. B., and V. Cardone, 1974: Observations of oceanic whitecaps and their relation to remote measurements of surface wind speed. *J. Geophys. Res.,* **79,** 444–452.

Sheets, R. C., 1969: Some mean hurricane soundings. *J. Appl. Meteor.,* **8,** 134–146.

St. Germain, K. M., C. T. Swift, and T. C. Grenfell, 1993: Determination of dielectric constant of young sea ice using microwave spectral radiometry. *J. Geophys. Res.,* **98,** 4675–4679.

Stogryn, A., 1972: The emissivity of sea foam at microwave frequencies. *J. Geophys. Res.,* **77,** 1658–1666.

Swift, C. T., and M. A. Goodberlet, 1992: Passive microwave remote sensing of the ocean. *Specialist Meeting on Microwave Radiometry and Remote Sensing Applications,* Boulder, CO, U.S. DOC/NOAA/ERL/WPL, 87–93.

——, D. C. Dehority, A. B. Tanner, and R. E. McIntosh, 1986: Passive microwave spectral emission from saline ice at C-band during

the growth phase. *IEEE Trans. Geosci. Remote Sens.,* **GE-24,** 840–848.

Tanner, A., C. T. Swift, and P. G. Black, 1987: Operational airborne remote sensing of wind speeds in hurricanes. Preprints, *17th Conf. Hurricane and Tropical Meteorology*, Miami, FL, Amer. Meteor. Soc., 385–387.

Tinga, W. R., W. A. G. Voss, and D. F. Blossey, 1973: Generalized approach to multiphase dielectric mixture theory. *J. Appl. Phys.,* **44,** 3897–3902.

Tran, N., D. Vandemark, C. S. Ruf, and B. Chapron, 2002: The dependence of nadir ocean surface emissivity on wind vector as measured with microwave radiometer. *IEEE Trans. Geosci. Remote Sens.,* **40,** 515–523.

Ulaby, F. W., R. K. Moore, and A. K. Fung, 1981: *Microwave Remote Sensing.* Vol. 1, *Active and Passive,* Artech House, 456 pp.

——, ——, and ——, 1986: *Microwave Remote Sensing.* Vol. 3, *Active and Passive,* Vol. 3. Artech House, 2162 pp.

U.S. Government Printing Office, 1976: *U.S. Standard Atmosphere, 1976.* U.S. Government Printing Office, 277 pp.

Webster, W. L. J., T. T. Wilheit, D. B. Ross, and P. Gloersen, 1976: Spectral characteristics of the microwave emission from a wind-driven foam-covered sea. *J. Geophys. Res.,* **81,** 3095–3099.

Wright, C. W., E. J. Walsh, D. Vandermark, W. B. Krabill, S. H. Houston, M. D. Powell, P. G. Black, and F. D. Marks, 2001: Hurricane directional wave spectrum spatial variation in the open ocean. *J. Phys. Oceanogr.,* **31,** 2472–2488.